ACS APPLIED MATERIALS & INTERFACES

www.acsami.org

Research Article

S-Doped Fe−N−C Single-Atom Nanozyme with Enhanced Oxidase-Like Activity for Colorimetric Detection of Serotonin

Published as part of ACS Applied Materials & Interfaces special issue "Nanozymes: Design, Mechanisms, and Applications".

Haoqiang Zhang,[1] Fuying Zhu,[1] Tao Song,[1] Yisong Ju, Congzhong Yang, Tianshu Zhang, Jiang Du, Liang Shi, Qiuling Yue,* Hui Wei,* and Xiaozhi Zhao*

Cite This: https://doi.org/10.1021/acsami.5c20971

Read Online

ACCESS | Metrics & More | Article Recommendations | Supporting Information

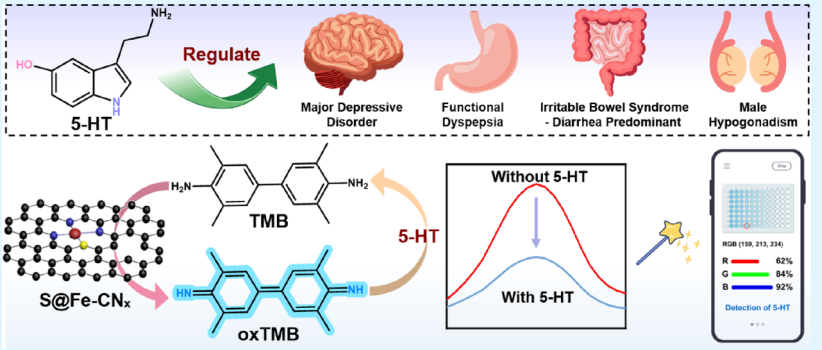

ABSTRACT: Serotonin (5-hydroxytryptamine, 5-HT) is a crucial neurotransmitter, the abnormal levels of which are closely associated with various neuropsychiatric disorders and male reproductive dysfunctions. In this study, a sulfur-doped Fe−N−C single-atom nanozyme (S@Fe-CN_x) was successfully synthesized, and its oxidase-like activity and catalytic mechanism were systematically investigated. The experimental results indicate that sulfur doping significantly enhanced Fe-CN_x oxygen activation capacity and catalytic kinetics by effectively optimizing the electronic structure of the FeN_x active centers. Leveraging its superior oxidase-like activity, we developed a H_2O_2-free colorimetric sensing method for the highly sensitive and selective detection of 5-HT. The method exhibited a good linear relationship between absorbance and 5-HT concentration in the range of 40 ng/mL to 10 μg/mL, achieving a low limit of detection of 6.0 ng/mL. The successful application of this method for detecting 5-HT in human serum samples demonstrates its great potential for practical use. Furthermore, we established a smartphone-based colorimetric detection platform that quantified 5-HT by correlating its concentration with the grayscale intensity of standard solution images captured by a smartphone. This approach provides a facile strategy for developing point-of-care testing platforms.

KEYWORDS: *S-doped single-atom nanozyme, oxidase-like activity, colorimetric sensing, serotonin, point-of-care testing*

1. INTRODUCTION

Serotonin (5-hydroxytryptamine, 5-HT) is a crucial monoamine neurotransmitter that exerts extensive regulatory functions in both the central and peripheral nervous systems.[1−4] It is involved in the modulation of a wide array of physiological and pathological processes, including mood, sleep, cognition, appetite, and reproductive functions.[5−9] Abnormal levels of 5-HT have been closely associated with numerous disorders, such as depression, anxiety, migraines, gastrointestinal dysfunction, and male infertility with common presentations like sexual dysfunction and poor sperm quality.[10−13] Consequently, there is a critical need to develop a 5-HT detection method with high sensitivity, selectivity, and reliability for applications in early diagnosis, monitoring of neuropsychiatric conditions, in-depth pathological research and clinical andrology assessment.[14,15]

At present, commonly employed techniques for 5-HT detection include high-performance liquid chromatography coupled with electrochemical detection (HPLC-EC),[16,17] liquid chromatography−mass spectrometry (LC-MS),[18,19] electrochemical sensors,[20,21] and fluorescent probes.[22,23]

Received: October 20, 2025
Revised: December 13, 2025
Accepted: December 17, 2025
Published: December 27, 2025

Among these, electrochemical methods are widely utilized owing to their operational simplicity, rapid response time, and instrumental portability.[24,25] Nonetheless, these methods are still hampered by several limitations, including susceptibility to electrode surface fouling, cumbersome electrode modification procedures, and insufficient anti-interference capability when dealing with complex biological samples.[26,27] As a result, there is a pressing need to develop alternative detection strategies that are characterized by simple sample pretreatment, strong anti-interference ability, and suitability for real sample applications.[28]

In recent years, nanozymes, functional nanomaterials that catalyze reactions like natural enzymes, have attracted considerable interest for applications in biosensing, environmental monitoring, and medical diagnostics. Their appeal lies in their high stability, potential for large-scale production, low cost, and tunable catalytic properties.[29−31] Among the diverse range of nanozymes, single-atom catalysts (SACs) have emerged as ideal candidates for emulating natural enzymes, due to their atomically dispersed active sites, maximal atom utilization efficiency, and unique electronic structures, all of which contribute to superior catalytic activity and selectivity.[14,32] However, most current research focuses on peroxidase (POD)-like nanozymes, which require hydrogen peroxide (H_2O_2) to function. Unfortunately, the practical applicability of H_2O_2 is limited because of its inherent instability and potential detrimental effects on biological environments.[33,34] In contrast, oxidase (OXD)-like nanozymes catalyze the oxidation of substrates directly utilizing molecular oxygen, without the need for H_2O_2, rendering them more suitable for biosensing applications.[35,36]

Although several OXD-like nanozymes have been reported in the literature, studies aimed at enhancing enzymatic activity through heteroatom doping strategies within Fe−N−C single-atom structures remain relatively scarce.[37,38] Sulfur (S) doping has been recognized as an effective approach for modulating the electronic structure of materials. It can optimize the charge distribution of carbon matrices, increase defect density, and fine-tune the coordination environment of metal centers, thereby holding great promise for significantly boosting the intrinsic catalytic activity of the material.[39−41]

Guided by this rationale, we innovatively designed and synthesized a sulfur-doped iron−nitrogen-carbon single-atom nanozyme (S@Fe-CN_x) and conducted a systematic investigation into its OXD-like catalytic performance and underlying mechanism. Our findings indicated that S doping effectively optimizes the electronic structure of the FeN_x active centers, leading to a notable improvement in oxygen activation capacity and overall catalytic kinetics. Furthermore, we developed, for the first time, a H_2O_2-free colorimetric sensing methodology based on this nanozyme for the highly sensitive and selective detection of 5-HT. This method was successfully applied to the analysis of human serum samples, demonstrating its practical utility. This study not only provides valuable insights for the design of high-performance single-atom nanozymes but also introduces a facile pathway for the rapid detection of neurotransmitters, thereby broadening the application horizons of nanozymes in bioanalysis and clinical diagnostics.[42]

2. EXPERIMENTAL SECTION

2.1. Chemical Reagents

Ferric chloride hexahydrate ($FeCl_3·6H_2O$) was obtained from Sinopharm Chemical Reagent Co., Ltd. (China). Melamine, L-Cysteine, L-Alanine, 3,3′,5,5′-tetramethylbenzidine (TMB), and sodium thiocyanate (NaSCN) were purchased from Shanghai Macklin Biochemical Technology Co., Ltd. (China). 5-Hydroxytryptamine (5-HT) and absolute ethanol were acquired from Shanghai Aladdin Industrial Co., Ltd. (China). All chemicals were of analytical grade and used without further purification.

2.2. Synthesis of S@Fe-CN_x and Fe-CN_x

For the typical synthesis of S@Fe-CN_x, melamine (2 g) and L-Cysteine (1 g) were dispersed in 30 mL of absolute ethanol. To this mixture, a solution of $FeCl_3·6H_2O$ (5 mg) in absolute ethanol was added dropwise under stirring. The reaction was allowed to proceed for 12 h at room temperature. The solvent was subsequently removed by evaporation at 80 °C. The resulting solid was subjected to a two-step pyrolysis process under a heating rate of 5 °C·min^{-1}: first heated to 550 °C and held for 3 h, then raised to 800 °C and maintained for 2 h, yielding S@Fe-CN_x. For the preparation of Fe-CN_x, the same procedure was followed except that L-Cysteine was replaced with L-Alanine.

2.3. Material Characterization

The morphology of the samples was characterized using transmission electron microscopy (TEM) on a Tecnai 12 microscope (Philips, Netherlands) operated at 120 kV and a JEM-2100 microscope (JEOL, Japan) operated at 200 kV. X-ray diffraction (XRD) patterns were recorded on a Rigaku Ultima III diffractometer (Japan) with Cu Kα radiation and a Bruker D8 advance diffractometer (Germany). UV−vis absorption spectra were acquired using a Cary UV−vis 100 spectrophotometer (Agilent Technologies, USA) and a SpectraMax M2e microplate reader (Molecular Devices, USA). Specific surface area was determined from N_2 adsorption−desorption isotherms measured at 77 K using a Kubo X1000 analyzer (Biaode, China). Elemental composition analysis was conducted via inductively coupled plasma atomic emission spectroscopy (ICP-AES) on a PerkinElmer Avio 500 spectrometer (USA). Surface chemical states were analyzed by X-ray photoelectron spectroscopy (XPS) using a PHI 5000 Versa Probe system (Ulvac-Phi, Japan) and a K-Alpha spectrometer (Thermo Fisher Scientific, USA).

2.4. Peroxidase-Like (POD-Like) and Oxidase-Like (OXD-Like) Activity Assays

POD-like activity was evaluated by monitoring the oxidation of TMB at 652 nm. The reaction mixture (1 mL) contained 30 μL of S@Fe-CN_x (1 mg/mL), 50 μL of TMB (10 mM), 100 μL of H_2O_2 (10 mM), and 820 μL of acetate buffer (0.1 M, pH 4.0). After incubation at 25 °C for 20 min, the absorbance was measured.

OXD-like activity was assessed under identical conditions except that H_2O_2 was omitted. The reaction system consisted of 30 μL of S@Fe-CN_x (1 mg/mL), 50 μL of TMB (10 mM), and 920 μL of acetate buffer (0.1 M, pH 4.0).

2.5. Evaluation of OXD-Like Activity of S@Fe-CN_x under Different Gas Atmospheres

The OXD-like activity of S@Fe-CN_x was evaluated by monitoring the oxidation of TMB in a 1 mL reaction system containing 15 μL of S@Fe-CN_x (1 mg/mL), 50 μL of TMB (10 mM), and 935 μL of acetate buffer (0.1 M, pH 4.0). To elucidate the role of oxygen in the catalytic process, the reaction was conducted under three distinct gas atmospheres. First, the activity was assessed under a continuous flow of oxygen to create an O_2-rich environment. Subsequently, an O_2-depleted condition was established by first removing surface oxygen with a deoxygenation bag, followed by continuous nitrogen purging for 20 min to eliminate dissolved oxygen. Finally, the reaction was also performed under ambient air as a reference.

https://doi.org/10.1021/acsami.5c20971
ACS Appl. Mater. Interfaces XXXX, XXX, XXX−XXX

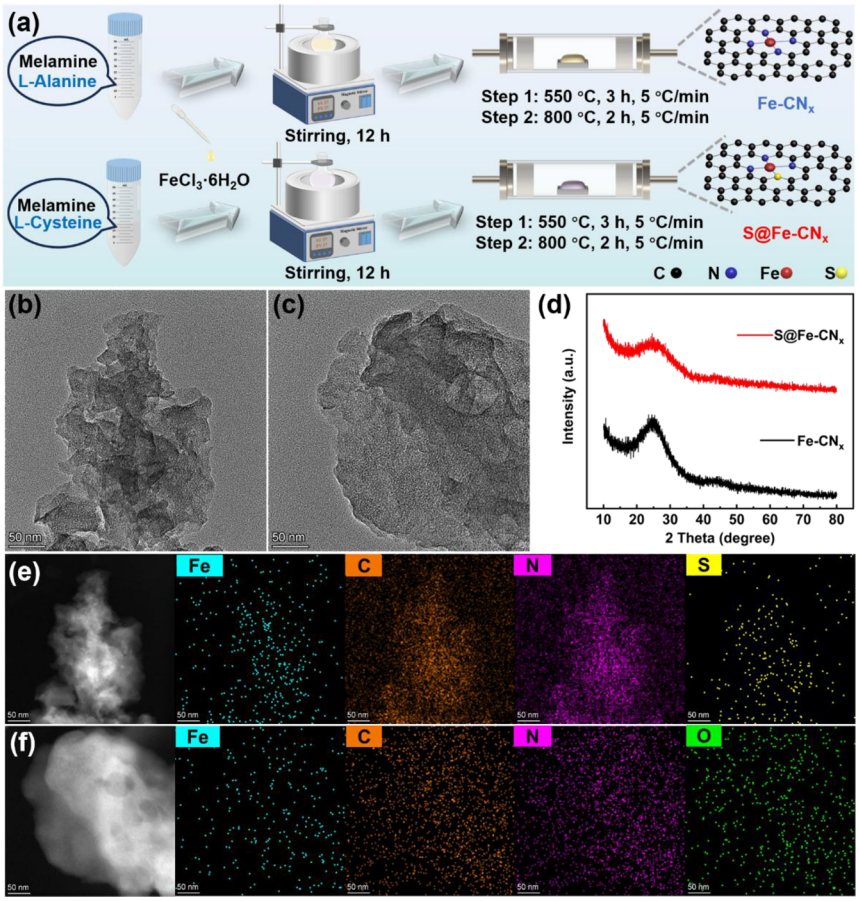

Figure 1. Synthesis and structural characterization of S@Fe-CN$_x$ and Fe-CN$_x$. (a) Schematic illustration of the synthesis route for S@Fe-CN$_x$ and Fe-CN$_x$. TEM images of (b) S@Fe-CN$_x$ and (c) Fe-CN$_x$. Scale bars: 50 nm. (d) X-ray diffraction (XRD) patterns of S@Fe-CN$_x$ and Fe-CN$_x$. EDS elemental mapping for (e) S@Fe-CN$_x$ and (f) Fe-CN$_x$, showing the homogeneous distribution of elements (C, N, Fe, and O or S). Scale bars: 50 nm.

2.6. Stability Tests

pH stability was evaluated by incubating S@Fe-CN$_x$ in buffer solutions of varying pH (3, 4, 5, 6, 7, or 8) for 2 h.

Thermal stability was assessed after treating S@Fe-CN$_x$ at different temperatures (0, 25, 50, and 75 °C) for 2 h.

Ionic strength stability was tested by incubating S@Fe-CN$_x$ in NaCl solutions (0, 0.5, 1.0, and 1.5 M) for 2 h.

Storage stability was examined by storing S@Fe-CN$_x$ (1 mg/mL) at room temperature and measuring its activity weekly over a period of 5 weeks.

The cycling stability of S@Fe-CN$_x$ was investigated to assess its reusability. Following each catalytic cycle of TMB oxidation, the S@Fe-CN$_x$ was recovered by centrifugation, thoroughly washed with acetate buffer, and then redispersed in a fresh reaction solution to initiate the next cycle. This procedure was repeated for multiple cycles, and the relative activity was recorded for each to determine the retention of catalytic performance.

All experiments were performed in triplicate.

2.7. Kinetic Analysis

Kinetic assays were carried out using varying concentrations of TMB as the substrate. A typical reaction system contained 2.5 μL of S@Fe-CN$_x$ (1 mg/mL), 235 μL of acetate buffer (0.1 M, pH 4.0), and 12.5 μL of TMB at different concentrations. The kinetic parameters, K_m and V_{max}, were derived by fitting the initial reaction rates to the Michaelis–Menten equation:

$$V = (V_{max} \times [S])/(K_m + [S])$$

2.8. Colorimetric Detection of 5-Hydroxytryptamine (5-HT)

The detection of 5-HT was performed by mixing 2 μL standard solution of 5-HT, 2 μL of S@Fe-CN$_x$ (1 mg/mL), 10 μL of TMB (10 mM), and 186 μL of acetate buffer (0.1 M, pH 4.0). After reaction at 25 °C for 20 min, the absorbance was measured at 652 nm. A calibration curve was constructed by plotting the absorbance values against the corresponding concentrations of 5-HT. In parallel, the oxTMB product was also subjected to a smartphone-based colorimetric analysis for potential point-of-care applications. The color was extracted, converted to grayscale values, and a linear fit was established between the grayscale intensity and the concentration of 5-HT.

2.9. Serum Sample Preparation and Pretreatment

Human venous blood (5 mL) was collected from healthy volunteers at Nanjing Drum Tower Hospital into vacuum blood collection tubes containing a clot activator. After obtaining informed consent from all participants, all procedures were approved by the Ethics Committee of Nanjing University (Approval No. 2024–988–01) and conducted in accordance with the World Health Organization's International Ethical Guidelines for Biomedical Research Involving Human Subjects. The blood samples were allowed to stand at room temperature for 30 min to facilitate complete coagulation and were subsequently centrifuged at 3000 rpm for 5 min. The resulting supernatant (serum) was carefully collected.

To mitigate potential matrix effects from complex biological components, the serum was subjected to a dilution-based pretreatment protocol. Specifically, the collected serum was diluted 100-fold with acetate buffer (0.1 M, pH 4.0). This diluted serum sample was then centrifuged again under the same conditions to remove any

https://doi.org/10.1021/acsami.5c20971
ACS Appl. Mater. Interfaces XXXX, XXX, XXX–XXX

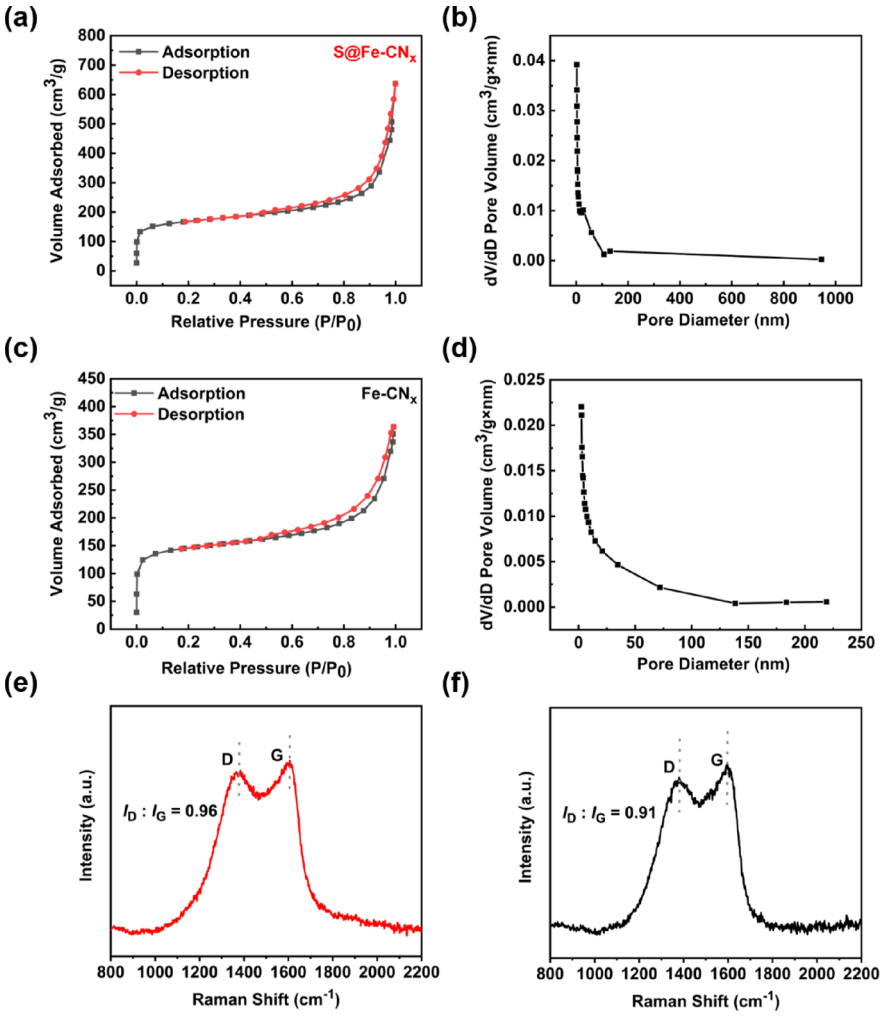

Figure 2. Textural properties of S@Fe-CN_x and Fe-CN_x. (a, c) N_2 adsorption−desorption isotherms and (b, d) the corresponding pore size distributions derived from the adsorption data. Raman spectra of (e) S@Fe-CN_x and (f) Fe-CN_x.

residual precipitated proteins. The clear supernatant was obtained and used as the treated sample solution for the subsequent 5-HT detection assay.

2.10. Detection of 5-HT in Human Serum

The detection of 5-HT in the pretreated human serum was performed using a standard addition method. Various concentrations of serotonin (5-HT) were spiked into the treated sample solution. The assay procedure involved mixing 2 μL of the spiked sample with 2 μL of S@Fe-CN_x (1 mg/mL), 10 μL of TMB (10 mM), and 186 μL of acetate buffer (0.1 M, pH 4.0). After incubation at 25 °C for 20 min, the absorbance was measured at a wavelength of 652 nm.

3. RESULTS AND DISCUSSION

S@Fe-CN_x and Fe-CN_x were synthesized via a wet impregnation method followed by a two-step pyrolysis under a nitrogen atmosphere (Figure 1a). In a typical procedure, melamine and L-Cysteine were homogeneously dispersed in anhydrous ethanol under magnetic stirring, followed by the dropwise addition of $FeCl_3 \cdot 6H_2O$ solution. Notably, an immediate color change from white to pale purple indicated rapid coordination between the metal ions and organic precursors. After continuous stirring, the resulting mixture was subjected to a stepwise pyrolysis protocol under nitrogen atmosphere: first at 550 °C to convert melamine into g-C_3N_4, and then at 800 °C to form an N, S-*co*-doped graphene-like carbon matrix coordinating atomically dispersed iron species. The final product, S@Fe-CN_x, exhibited an iron loading of 1.07 wt % as quantified by ICP-OES. For comparison, Fe-CN_x was prepared using an identical procedure, except that L-Cysteine was replaced with L-Alanine. Zeta potential measurements revealed that all as-synthesized samples possessed negatively charged surfaces, providing insight into their surface properties. Interestingly, S@Fe-CN_x showed a more negative potential than Fe-CN_x (Figure S1), implying that sulfur doping further enhanced the surface electronegativity.

The morphology and structural features of the catalysts were further examined. Transmission electron microscopy (TEM) images revealed that both S@Fe-CN_x and Fe-CN_x exhibited uniform, particle-free morphologies without discernible crystalline aggregates or nanoparticles (Figure 1**b, c**). Consistently, X-ray diffraction (XRD) patterns further confirmed the structural homogeneity of the materials (Figure 1d), showing only broad and weak diffraction peaks at 22.8° and 43.9°, which correspond to the (120) and (111) crystal planes of disordered graphitic carbon. The absence of diffraction signals attributable to metallic iron or its compounds indicated a highly dispersed state of the iron species.[43−46] Moreover, compared to Fe-CN_x, S@Fe-CN_x exhibited broader and weaker diffraction peaks, suggesting that sulfur doping introduced additional structural defects.[47] This conclusion

https://doi.org/10.1021/acsami.5c20971
ACS Appl. Mater. Interfaces XXXX, XXX, XXX−XXX

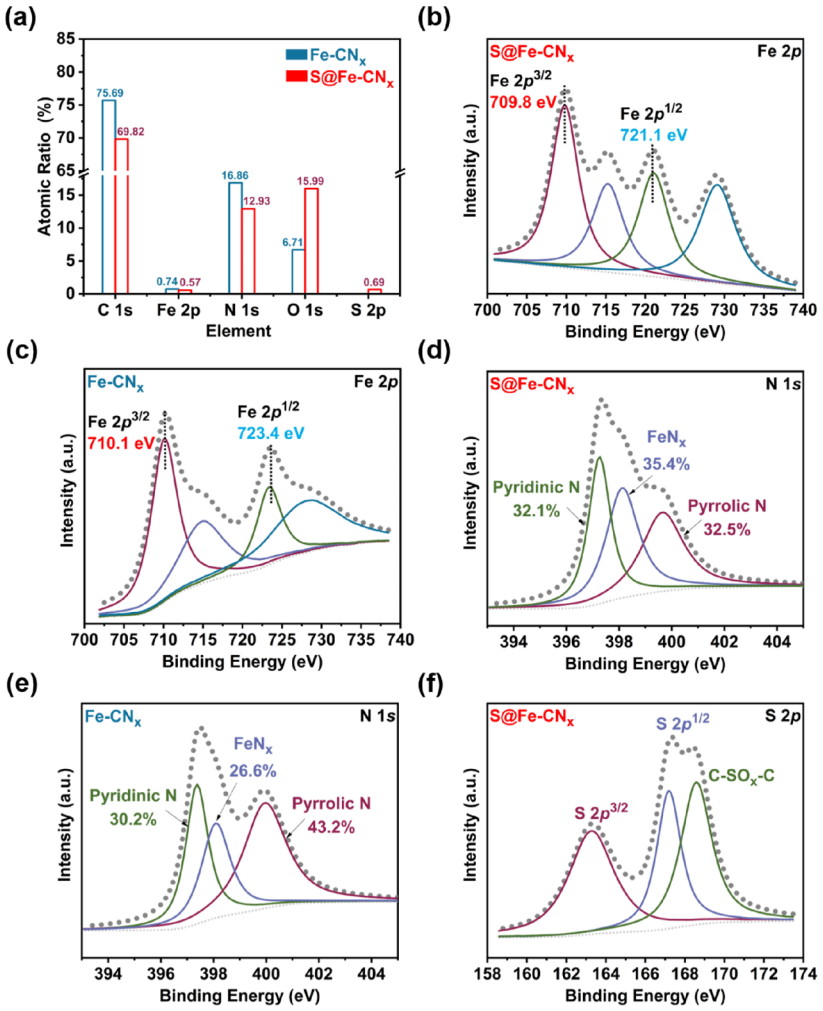

Figure 3. X-ray photoelectron spectroscopy (XPS) analysis of S@Fe-CN$_x$ and Fe-CN$_x$. (a) XPS survey spectra. High-resolution Fe 2*p* spectra of (b) S@Fe-CN$_x$ and (c) Fe-CN$_x$. Deconvoluted N 1*s* spectra of (d) S@Fe-CN$_x$ and (e) Fe-CN$_x$. (f) High-resolution S 2*p* spectrum of S@Fe-CN$_x$.

was further corroborated by elemental mapping analysis, which revealed a homogeneous distribution of Fe, N, C, O, and S in both S@Fe-CN$_x$ and Fe-CN$_x$, with no detectable iron aggregation (Figure 1**e, f**).

We further investigated the porous structure and defect nature of the materials. Nitrogen adsorption−desorption measurements indicated that S@Fe-CN$_x$ possessed a specific surface area of 599.5 $m^2 \cdot g^{-1}$, which is higher than that of Fe-CN$_x$ (516.4 $m^2 \cdot g^{-1}$) (Figure 2**a, b**). The corresponding isotherms revealed that both materials feature a combined microporous and mesoporous structure (Figure 2**c, d**). Additionally, Raman spectroscopy exhibited that the I_D/I_G ratio increased from 0.91 for Fe-CN$_x$ to 0.96 for S@Fe-CN$_x$ (Figure 2**e, f**), indicating that sulfur doping further promoted structural disorder in the carbon matrix. Collectively, the structural advantages arising from the larger surface area, developed porosity, and higher defect density contribute to increased exposure of active sites and improved substrate accessibility.[48]

To further elucidate the impact of sulfur doping on the valence state and local electronic environment of the iron sites, X-ray photoelectron spectroscopy (XPS) analysis was conducted. The survey spectra (Figure 3a) confirm the presence of Fe, C, N, O, and S in S@Fe-CN$_x$ (atomic%: Fe 0.57, C 69.82, N 12.93, O 15.99, S 0.69), while Fe-CN$_x$ is primarily composed of Fe, C, N, and O (atomic%: Fe 0.74, C 75.69, N 16.86, O 6.71), confirming successful sulfur doping in S@Fe-CN$_x$. High-resolution scans of the Fe 2*p*, N 1*s*, and S 2*p* regions were subsequently performed. The Fe 2*p* spectra (Figure 3**b, c**) reveal that iron exists predominantly in the Fe^{2+} state in both materials. Notably, a blueshift in the binding energy of the Fe 2*p* peaks is observed for S@Fe-CN$_x$ compared to Fe-CN$_x$, indicating that the iron species in S@Fe-CN$_x$ are in a more reduced state. This suggests that sulfur doping (with its lower electronegativity than nitrogen) increases the electron density around the iron centers, facilitating electron transfer during catalysis.[43] The deconvoluted N 1*s* spectra (Figure 3**d, e**) show the presence of FeN$_x$, pyrrolic N, and pyridinic N species in both catalysts. The identification of FeN$_x$ coordination serves as direct evidence for the atomic dispersion of iron within the N-coordinated environment. Furthermore, the content of FeN$_x$ species is significantly higher in S@Fe-CN$_x$ (35.4%) than in Fe-CN$_x$ (26.6%), implying that the incorporation of sulfur favors the anchoring of iron atoms by nitrogen sites, leading to the formation of more FeN$_x$ active sites. Finally, the high-resolution S 2*p* spectrum of S@Fe-CN$_x$ (Figure 3f) is dominated by two characteristic peaks at ∼ 163.3 eV and ∼ 167.2 eV, corresponding to the S $2p^{3/2}$ and S $2p^{1/2}$ spin orbit doublet of C−S−C species, respectively.[49] An additional peak observed at ∼ 168.6 eV is attributable to

https://doi.org/10.1021/acsami.5c20971
ACS Appl. Mater. Interfaces XXXX, XXX, XXX−XXX

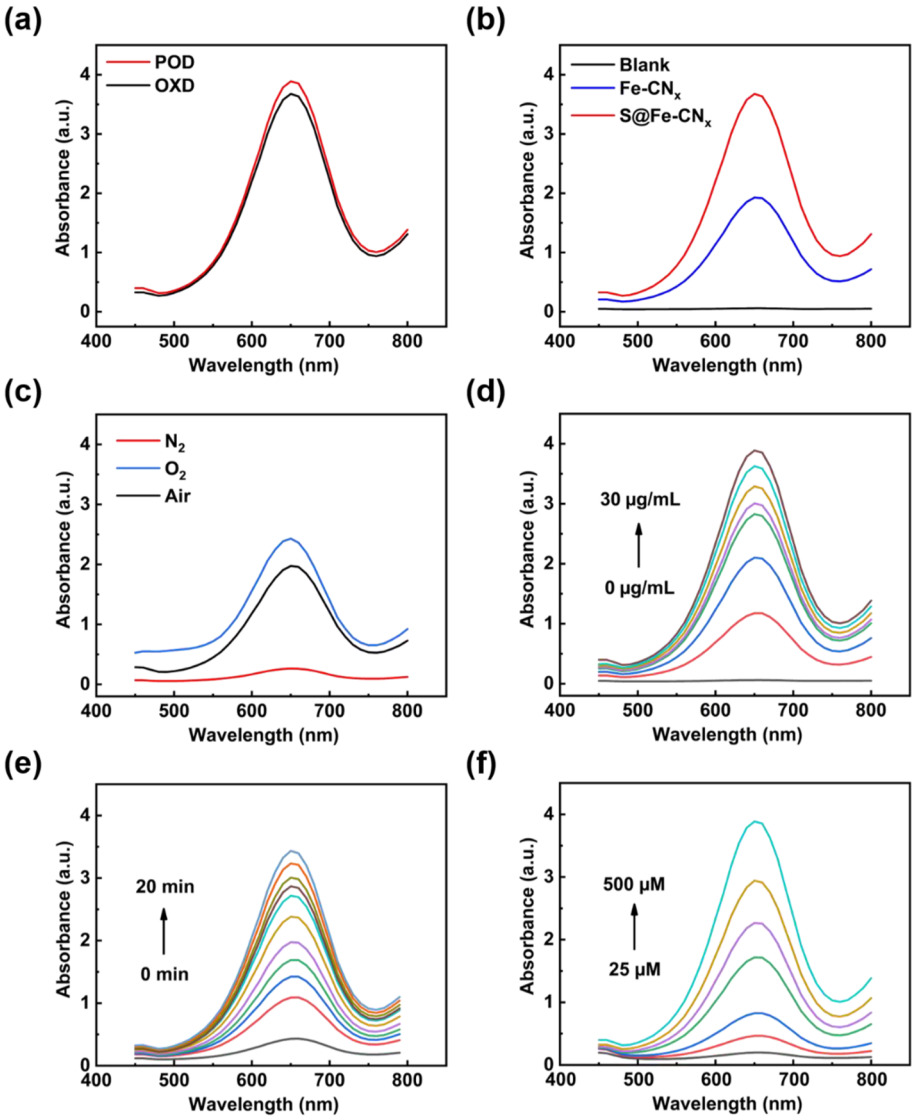

Figure 4. Catalytic performance and mechanism study of S@Fe-CN_x. (a) Absorbance of oxidized TMB catalyzed by S@Fe-CN_x in the presence or absence of H_2O_2. (b) Comparison of OXD-like activity between S@Fe-CN_x and Fe-CN_x. (c) Catalytic activity of S@Fe-CN_x under different atmospheres (N_2, Air, O_2). (d–f) Catalytic efficiency of S@Fe-CN_x shows a positive correlation with increasing (d) catalyst concentration (0, 2.5, 5, 10, 15, 20, 25, 30 μg/mL), (e) reaction time (0–20 min, 2 min interval), and (f) substrate (TMB) concentration (25, 50, 100, 200, 300, 400, 500 μM).

oxidized sulfur species (-C–SO_x-C–), likely formed due to the surface oxidation of some sulfur sites upon air exposure.

To further evaluate the specific enhancement of sulfur doping on the catalytic performance of S@Fe-CN_x, the POD-like and OXD-like activities were first assessed using the TMB colorimetric assay. As shown in Figure 4a, the reaction activity showed no significant change in the presence or absence of H_2O_2, indicating that OXD-like activity dominates in S@Fe-CN_x, enabling efficient activation of atmospheric oxygen. Compared with Fe-CN_x, S@Fe-CN_x exhibited stronger OXD-like activity, suggesting that sulfur doping enhances the material's ability to activate oxygen (Figure 4b). Atmosphere control experiments revealed that the catalytic activity was suppressed under N_2 atmosphere but enhanced in an O_2-rich environment (Figure 4c), further confirming its efficient activation of oxygen. In addition, a systematic evaluation showed that the catalytic efficiency of S@Fe-CN_x increased with higher catalyst concentration (0–30 μg/mL), longer reaction time (0–20 min), and increased substrate concentration (25–500 μM), demonstrating a positive correlation (Figure 4**d-f**). Given that nanozymes are expected to possess advantages such as high stability, tolerance to harsh pH conditions, and long storage time compared to natural enzymes, we further evaluated the stability of S@Fe-CN_x. The results indicated that S@Fe-CN_x retained over 85% of its initial activity under a wide range of pH conditions (3–8), high temperature (100 °C), high ionic strength (≤1.5 M NaCl), as well as extended storage (35 days), and four catalytic cycles, demonstrating excellent environmental adaptability, storage stability, and recyclability (Figure S2 **and** Figure S3), thereby laying the foundation for its practical applications.

Additionally, the catalytic activity of S@Fe-CN_x was also tested with other common chromogenic substrates, such as *o*-phenylenediamine (OPD) and 2,2′-azino-bis(3-ethylbenzothiazoline-6-sulfonic acid) (ABTS). Comparative analysis revealed that TMB serves as the optimal substrate for S@Fe-CN_x, as its oxidation was significantly more pronounced than that of OPD or ABTS (Figure 5a). This substrate preference is

https://doi.org/10.1021/acsami.5c20971
ACS Appl. Mater. Interfaces XXXX, XXX, XXX–XXX

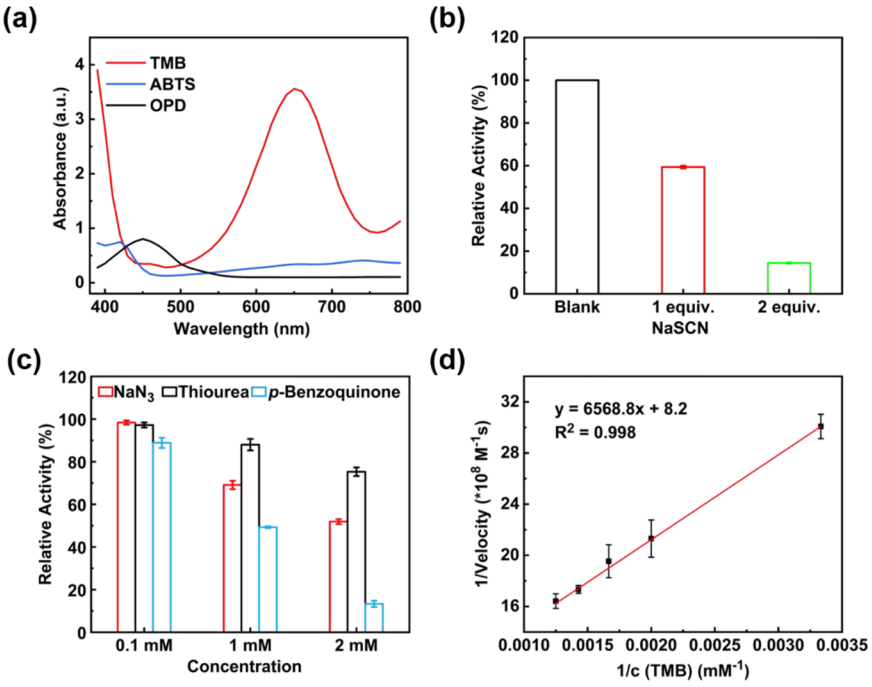

Figure 5. Substrate specificity, active site verification, and catalytic mechanism of S@Fe-CN$_x$. (a) Substrate specificity assay using TMB, OPD, and ABTS. (b) Poisoning of Fe−N$_x$ sites by sodium thiocyanate (NaSCN). (c) Effects of various radical scavengers on the catalytic activity (thiourea: $^{\bullet}$OH scavenger; *p*-benzoquinone: $O_2^{\bullet-}$ scavenger; sodium azide: $^1O_2$ scavenger). (d) Lineweaver−Burk plot of S@Fe-CN$_x$ for TMB oxidation. The corresponding kinetic parameters (K_m and V_{max}) are summarized in Table S1. Error bars represent the standard deviation (n = 3).

attributed to the combined effects of electrostatic interactions and intrinsic substrate reactivity. In the acidic medium (pH 4.0), electrostatic repulsion hinders the interaction between the negatively charged S@Fe-CN$_x$ and anionic ABTS (Figure S1), whereas both TMB and OPD are favorably attracted. The superior catalytic efficiency of S@Fe-CN$_x$ toward TMB is ultimately due to its stronger electron-donating dimethyl amino groups, which increase the electron density on the aromatic ring, thereby significantly enhancing its oxidation efficiency.[50−53]

To further confirm the critical role of Fe−N$_x$ sites in the OXD-like activity, a poisoning experiment using sodium thiocyanate (NaSCN) was conducted.[54,55] With increasing dosage of the poisoning agent, the Fe−N$_x$ sites were gradually blocked, leading to a significant decrease in catalytic activity, which confirmed that Fe−N$_x$ serves as the key catalytic active center (Figure 5b). Due to the effective activation of oxygen by S@Fe-CN$_x$, highly reactive oxygen species (ROS) were generated, contributing to its excellent OXD-like activity. Accordingly, we investigated the types of ROS produced during the catalytic process. By adding specific radical scavengers, thiourea for $^{\bullet}$OH, *p*-benzoquinone for $O_2^{\bullet-}$, and sodium azide for $^1O_2$, we found that superoxide anion ($O_2^{\bullet-}$) plays a dominant role in the catalysis (Figure 5c). Based on the OXD-like activity of S@Fe-CN$_x$, a quantitative evaluation was performed. Analysis of the Michaelis−Menten kinetics curves and Lineweaver−Burk plots (Figure 5d) revealed that the K_m and V_{max} of S@Fe-CN$_x$ for TMB are 0.8 mM and 12.2 × 10^{-8} M·s^{-1}, respectively, indicating strong substrate affinity and high reaction rate in mimicking OXD-like performance, which surpasses those of most reported nanozymes (Table S1).

Based on the excellent OXD-like activity of S@Fe-CN$_x$, we developed a colorimetric sensing platform for the detection of serotonin (5-HT). The detection mechanism relies on the inhibitory effect of 5-HT on the OXD-like activity of S@Fe-CN$_x$. Specifically, in the presence of dissolved oxygen, S@Fe-CN$_x$ catalyzes the oxidation of TMB to produce a blue-colored product, oxTMB, which exhibits a characteristic absorption peak at 652 nm. Meanwhile, 5-HT, as a reducing substance, can react with reactive oxygen species (such as $O_2^{\bullet-}$) generated during the catalytic process, thereby suppressing the formation of oxTMB and resulting in a decrease in absorbance (Figure 6a). By measuring the change in absorbance, quantitative detection of 5-HT can be achieved. A standard curve was established between the absorbance of oxTMB at 652 nm and the concentration of 5-HT, showing a good linear relationship from 40 ng/mL to 10 μg/mL. The fitted equation was y = −0.0000500x + 1.13 (R^2 = 0.992) (Figure 6**b, c**). The limit of detection (LOD, S/N = 3) was calculated to be 6.0 ng/mL. Compared with existing methods for 5-HT detection, this approach demonstrates significant advantages in terms of sensitivity (Table S2).

The selectivity of the sensor was evaluated against various potential interferents. As shown in Figure 6d, 5-HT caused a distinct inhibition, while substances including hormones (hydrocortisone and progesterone), androgens (drostanolone and dihydrotestosterone), glucose, and amino acids (L-cysteine and glutamic acid) produced negligible inhibition at the same concentration. Notably, L-tryptophan, the direct biosynthetic precursor of 5-HT, showed almost no interference, and tryptamine, which shares the closest indole structure, exhibited only a minor effect. These results confirm the excellent specificity of the sensing platform for 5-HT detection.

To further elucidate the molecular mechanism by which 5-HT inhibits the OXD-like activity of S@Fe-CN$_x$, we conducted electron spin resonance (ESR) spectroscopy using 5,5-dimethyl-1-pyrroline N-oxide (DMPO) as a spin trap to monitor the generation of $O_2^{\bullet-}$ under different conditions. As

https://doi.org/10.1021/acsami.5c20971
ACS Appl. Mater. Interfaces XXXX, XXX, XXX−XXX

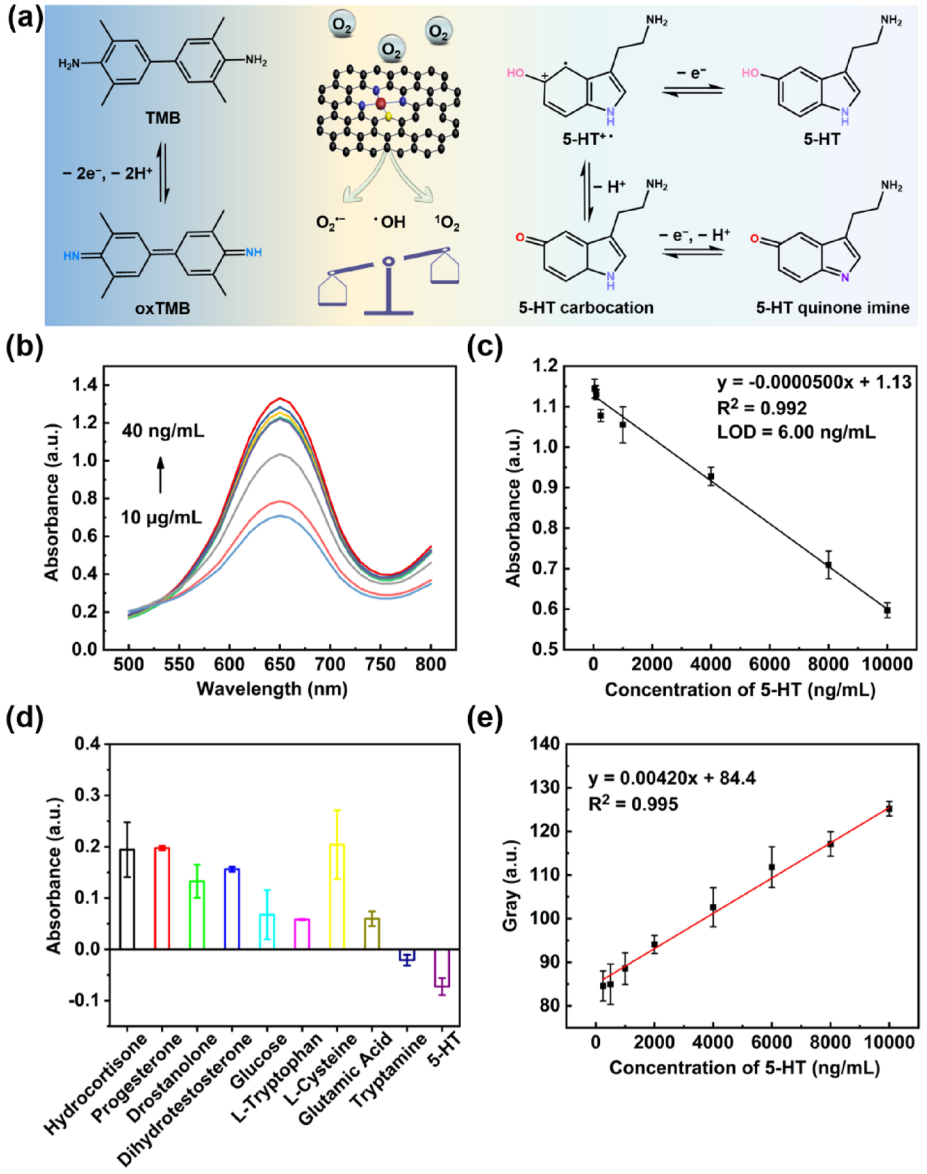

Figure 6. Detection of 5-HT using an S@Fe-CN$_x$-based colorimetric sensor. (a) Schematic illustration of the sensing mechanism. (b) Absorbance spectra and (c) the corresponding calibration curve for 5-HT detection (40, 80, 100, 250, 1000, 4000, 8000, 10,000 ng/mL). The inset in (c) shows the linear regression equation. (d) Selectivity of the sensor toward 5-HT against various potential interfering substances. (e) Grayscale analysis of the colorimetric responses catalyzed by S@Fe-CN$_x$ at different 5-HT concentrations. Error bars represent the standard deviation (n = 3).

illustrated in Figure S4, the characteristic sextet ESR signal of the DMPO-•OOH adduct was clearly observed in the presence of S@Fe-CN$_x$ (Black), confirming its capability to activate oxygen and generate $O_2^{\bullet-}$. Notably, when S@Fe-CN$_x$ was preincubated with 5-HT and then collected via centrifugation and washing (denoted as T-S@Fe-CN$_x$), the ESR signal intensity significantly decreased, indicating that 5-HT can interact with the FeN$_x$ active sites, thereby reducing its ability to generate $O_2^{\bullet-}$. Furthermore, upon direct addition of 5-HT into the S@Fe-CN$_x$ reaction system, the $O_2^{\bullet-}$ signal was almost completely quenched, suggesting that 5-HT also acts as an effective $O_2^{\bullet-}$ scavenger. These results collectively demonstrate that 5-HT exerts its inhibitory effect through a dual mechanism: (1) direct interaction with the FeN$_x$ active sites of S@Fe-CN$_x$, and (2) efficient scavenging of the generated $O_2^{\bullet-}$ radicals.

To further validate the reliability and practical utility of the developed method, we established a smartphone-based colorimetric detection system. Calibration with standard solutions revealed a robust linear relationship between 5-HT concentration and the grayscale intensity measured by the mobile device (y = 0.00420x + 84.4, Figure 6e). Subsequent comparison of smartphone-derived grayscale values with absorbance readings from a conventional UV−vis spectrophotometer showed a strong correlation (z = − 0.0118y + 2.09, R^2 = 0.984, Figure S5), confirming that the hand-held imaging approach faithfully reproduces instrumental readings and highlighting its potential for point-of-care applications.

The clinical applicability of the platform was further assessed through parallel analysis of human serum samples using both the smartphone system and the reference spectrophotometer. As summarized in Table S3, the two data sets showed close agreement across all samples, with relative standard deviations consistently below 5% (n = 3). Given the excellent repeatability, which validates the accuracy of the smartphone detection protocol, we conclude that the integrated S@Fe-CN$_x$

https://doi.org/10.1021/acsami.5c20971
ACS Appl. Mater. Interfaces XXXX, XXX, XXX−XXX

and mobile colorimetry platform is a robust, precise, and field-deployable tool for on-site 5-HT quantification in complex biological matrices.

4. CONCLUSIONS

In this study, a sulfur-doped iron single-atom nanozyme (S@Fe-CN_x) was successfully synthesized via wet impregnation and high-temperature pyrolysis. Structural characterization confirmed that sulfur doping optimizes the electronic structure of the FeN_x active sites, leading to a remarkable enhancement in oxidase-like activity. Based on this, we constructed a highly selective and sensitive H_2O_2-free colorimetric sensing platform and successfully applied it to the analysis of 5-HT in complex human serum samples. Additionally, a preliminary smartphone-based colorimetric analysis method was established, validating the linear correlation between 5-HT concentration and grayscale value in a standard solution system, which highlights the application prospect of this method in the field of portable and point-of-care testing. This study not only provides new insights for the design of high-performance single atom nanozymes but also offers a facile strategy that extends neurotransmitter detection from conventional instrumental analysis toward on-site rapid testing.

■ ASSOCIATED CONTENT

Data Availability Statement

All data needed to evaluate the conclusions in the paper are present in the paper and/or the Supporting Information.

Supporting Information

The Supporting Information is available free of charge at https://pubs.acs.org/doi/10.1021/acsami.5c20971.

Zeta potential measurements; stability tests of the S@Fe-CN_x material; electron spin resonance (ESR) spectroscopic analysis for investigating the molecular mechanism of serotonin-induced inhibition of TMB oxidation; comparative validation of the smartphone-based colorimetric platform and spectrophotometry for serotonin detection; comparison of kinetic parameters of oxidase-like activity among different nanozymes; linear range and limit of detection for serotonin determination; recovery rates of spiked human serum samples analyzed by smartphone-based grayscale analysis and UV−vis absorption spectrophotometry (PDF)

■ AUTHOR INFORMATION

Corresponding Authors

Qiuling Yue − *Department of Andrology, Nanjing Drum Tower Hospital, The Affiliated Hospital of Nanjing University Medical School, Nanjing 210008, China; Department of Andrology, Nanjing Drum Tower Hospital Clinical College of Nanjing University of Chinese Medicine, Nanjing, Jiangsu 210008, China*; Email: yulychina@163.com

Hui Wei − *Department of Andrology, Nanjing Drum Tower Hospital, The Affiliated Hospital of Nanjing University Medical School, Nanjing 210008, China; Department of Biomedical Engineering, College of Engineering and Applied Sciences, Nanjing National Laboratory of Microstructures Jiangsu Key Laboratory of Artificial Functional Materials, Nanjing University, Nanjing, Jiangsu 210023, China;* orcid.org/0000-0003-0870-7142; Email: weihui@nju.edu.cn

Xiaozhi Zhao − *Department of Andrology, Nanjing Drum Tower Hospital, The Affiliated Hospital of Nanjing University Medical School, Nanjing 210008, China; Department of Andrology, Nanjing Drum Tower Hospital Clinical College of Nanjing University of Chinese Medicine, Nanjing, Jiangsu 210008, China;* orcid.org/0000-0002-4265-9730; Email: zhaoxz@nju.edu.cn

Authors

Haoqiang Zhang − *Department of Andrology, Nanjing Drum Tower Hospital, The Affiliated Hospital of Nanjing University Medical School, Nanjing 210008, China; Department of Andrology, Nanjing Drum Tower Hospital Clinical College of Nanjing University of Chinese Medicine, Nanjing, Jiangsu 210008, China;* orcid.org/0009-0001-2901-3724

Fuying Zhu − *Department of Andrology, Nanjing Drum Tower Hospital, The Affiliated Hospital of Nanjing University Medical School, Nanjing 210008, China; Department of Biomedical Engineering, College of Engineering and Applied Sciences, Nanjing National Laboratory of Microstructures Jiangsu Key Laboratory of Artificial Functional Materials, Nanjing University, Nanjing, Jiangsu 210023, China;* orcid.org/0009-0006-1358-2435

Tao Song − *Department of Andrology, Nanjing Drum Tower Hospital, The Affiliated Hospital of Nanjing University Medical School, Nanjing 210008, China*

Yisong Ju − *Department of Andrology, Nanjing Drum Tower Hospital, The Affiliated Hospital of Nanjing University Medical School, Nanjing 210008, China; Department of Andrology, Nanjing Drum Tower Hospital Clinical College of Nanjing University of Chinese Medicine, Nanjing, Jiangsu 210008, China*

Congzhong Yang − *Department of Biomedical Engineering, College of Engineering and Applied Sciences, Nanjing National Laboratory of Microstructures Jiangsu Key Laboratory of Artificial Functional Materials, Nanjing University, Nanjing, Jiangsu 210023, China;* orcid.org/0009-0003-8124-4719

Tianshu Zhang − *Department of Andrology, Nanjing Drum Tower Hospital, The Affiliated Hospital of Nanjing University Medical School, Nanjing 210008, China*

Jiang Du − *Department of Biomedical Engineering, College of Engineering and Applied Sciences, Nanjing National Laboratory of Microstructures Jiangsu Key Laboratory of Artificial Functional Materials, Nanjing University, Nanjing, Jiangsu 210023, China*

Liang Shi − *Department of Andrology, Nanjing Drum Tower Hospital, The Affiliated Hospital of Nanjing University Medical School, Nanjing 210008, China*

Complete contact information is available at: https://pubs.acs.org/10.1021/acsami.5c20971

Author Contributions

[1]H.Z., F.Z. and T.S. contributed equally to this work.

Author Contributions

H.Z., F.Z., and T.S. contributed equally to this work. The specific contributions are as follows: H.Z. performed investigation, data curation, and visualization. F.Z. was in

https://doi.org/10.1021/acsami.5c20971
ACS Appl. Mater. Interfaces XXXX, XXX, XXX−XXX

charge of methodology, investigation, data curation, visualization, and writing—original draft. T.S. performed conceptualization, supervision, and data analysis. Y.J. was in charge of material characterization and analysis. C.Y. performed experimental validation. T.Z. performed resource gathering and experimental support. J.D. performed electron microscopy characterization and analysis. L.S. was in charge of partial experiments and discussion. Q.Y. performed funding acquisition and supervision. H.W. and X.Z. performed conceptualization, funding acquisition, supervision, and writing—review & editing. All authors have read and approved the final version of the manuscript.

Notes

The authors are accountable for all aspects of the work in ensuring that questions related to the accuracy or integrity of any part of the work are appropriately investigated and resolved.

The authors declare no competing financial interest.

■ ACKNOWLEDGMENTS

This work was supported by the National Natural Science Foundation of China (82070703 and 92168112). The authors also extend their grateful acknowledgement to Xiaomiao Cui and Jiawen Han for their valuable contributions to this work.

■ REFERENCES

(1) Furness, J. B. The enteric nervous system and neurogastroenterology. *Nat. Rev. Gastro. Hepat.* **2012**, *9* (5), 286−294.

(2) Li, Y.; Zhong, W.; Wang, D.; Feng, Q.; Liu, Z.; Zhou, J.; Jia, C.; Hu, F.; Zeng, J.; Guo, Q.; et al. Serotonin neurons in the dorsal raphe nucleus encode reward signals. *Nat. Commun.* **2016**, *7* (1), 10503.

(3) Jones, L. A.; Sun, E. W.; Martin, A. M.; Keating, D. J. The ever-changing roles of serotonin. *Int. J. Biochem. Cell Biol.* **2020**, *125*, No. 105776.

(4) Cai, X.; Liu, H.; Feng, B.; Yu, M.; He, Y.; Liu, H.; Liang, C.; Yang, Y.; Tu, L.; Zhang, N.; et al. A D2 to D1 shift in dopaminergic inputs to midbrain 5-HT neurons causes anorexia in mice. *Nat. Neurosci.* **2022**, *25* (5), 646−658.

(5) Karayol, R.; Medrihan, L.; Warner-Schmidt, J. L.; Fait, B. W.; Rao, M. N.; Holzner, E. B.; Greengard, P.; Heintz, N.; Schmidt, E. F. Serotonin receptor 4 in the hippocampus modulates mood and anxiety. *Mol. Psychiatry.* **2021**, *26* (6), 2334−2349.

(6) Aaldijk, E.; Vermeiren, Y. The role of serotonin within the microbiota-gut-brain axis in the development of Alzheimer's disease: A narrative review. *Ageing Res. Rev.* **2022**, *75*, No. 101556.

(7) Salvan, P.; Fonseca, M.; Winkler, A. M.; Beauchamp, A.; Lerch, J. P.; Johansen-Berg, H. Serotonin regulation of behavior via large-scale neuromodulation of serotonin receptor networks. *Nat. Neurosci.* **2023**, *26* (1), 53−63.

(8) Sutanto, C. N.; Xia, X.; Heng, C. W.; Tan, Y. S.; Lee, D. P. S.; Fam, J.; Kim, J. E. The impact of 5-hydroxytryptophan supplementation on sleep quality and gut microbiota composition in older adults: A randomized controlled trial. *Clin. Nutr.* **2024**, *43* (3), 593−602.

(9) Jiménez-Trejo, F.; Tapia-Rodríguez, M.; Cerbón, M.; Kuhn, D. M.; Manjarrez-Gutiérrez, G.; Mendoza-Rodríguez, C. A.; Picazo, O. Evidence of 5-HT components in human sperm: implications for protein tyrosine phosphorylation and the physiology of motility. *Reproduction* **2012**, *144* (6), 677−685.

(10) Liu, J.; Zhang, W.; Chen, Q.; He, M.; Xian, Y.; Le, S.; Jiang, Y.; Zhang, J.; Chen, S.; Wang, L. Melatonin promotes tendon-derived stem cells differentiation and inhibits oxidative stress in trauma-induced heterotopic ossification. *Eur. Cell. Mater.* **2025**, *49*, 55−70.

(11) Kendig, D. M.; Grider, J. R. Serotonin and colonic motility. *Neurogastroenterol. Motil.* **2015**, *27* (7), 899−905.

(12) Walsh, J. J.; Christoffel, D. J.; Heifets, B. D.; Ben-Dor, G. A.; Selimbeyoglu, A.; Hung, L. W.; Deisseroth, K.; Malenka, R. C. 5-HT release in nucleus accumbens rescues social deficits in mouse autism model. *Nature* **2018**, *560* (7720), 589−594.

(13) Boyer, E. W.; Shannon, M. The Serotonin Syndrome. *N. Engl. J. Med.* **2005**, *352* (11), 1112−1120.

(14) Sun, L.; Xu, H.; Bai, Y.; Chang, L.; Gao, J.; Zhao, M.; Huang, A. T.; Ma, L.; Lei, Y.; Kang, F.; et al. Vanadium single atoms embedded in MoS_2 enabled gut-brain axis neurotransmitter detection at pM levels. *Small* **2024**, *20* (39), No. 2307410.

(15) Sun, C.; Liu, X.; Zhuo, H.; He, X.; Ge, Z.; Zhang, Y.; Li, Z.; Xiong, Q. A post-modified lanthanide metal-organic frameworks as ratiometric luminescent sensor for the visual detection of 5-hydroxytryptamine. *J. Hazard. Mater.* **2025**, *484*, No. 136793.

(16) Florensa-Zanuy, E.; Garro-Martínez, E.; Adell, A.; Castro, E.; Díaz, Á.; Pazos, Á.; Mac-Dowell, K. S.; Martín-Hernández, D.; Pilar-Cuéllar, F. Cannabidiol antidepressant-like effect in the lipopolysaccharide model in mice: Modulation of inflammatory pathways. *Biochem. Pharmacol.* **2021**, *185*, No. 114433.

(17) Jalal, K.; Khan, F.; Nawaz, S.; Afroz, R.; Khan, K.; Ali, S. B.; Hao, L.; Khan, S. A.; Kazi, M.; Uddin, R.; et al. Anxiolytic, antinociceptive and body weight reducing effects of L-lysine in rats: Relationship with brain serotonin an in-*vivo* and in-silico study. *Biomed. Pharmacother.* **2022**, *152*, No. 113235.

(18) van Zundert, S. K. M.; van Egmond, N. C. M.; van Rossem, L.; Willemsen, S. P.; Griffioen, P. H.; van Schaik, R. H. N.; Mirzaian, M.; Steegers-Theunissen, R. P. M. First trimester maternal tryptophan metabolism and embryonic and fetal growth: the rotterdam periconceptional cohort (predict study). *Hum. Reprod.* **2024**, *39* (5), 912−922.

(19) Guła, Z.; Krzyściak, W.; Kuszmiersz, P.; Bystrowska, B.; Korkosz, M. Higher serotonin levels among patients with rheumatoid arthritis, psoriatic arthritis, and axial spondyloarthritis compared to healthy controls assessed by liquid chromatography-tandem mass spectrometry (LC-MS). *Rheumatol. Int.* **2025**, *45* (1), 17.

(20) Mukundan, G.; Ganapathy, N.; Badhulika, S. ZnO nanoparticles-copper metal-organic framework composite on 3D porous nickel foam: a novel electrochemical sensing platform to detect serotonin in blood serum. *Nanotechnology* **2023**, *34* (40), No. 405501.

(21) Veerapandian, M.; Chandran, M.; Dhanasekaran, B.; Govindaraju, S.; Yun, K. Fabrication of Zn-Cu bimetallic MOF-based flexible electrodes for serotonin detection in serum. *Analyst* **2025**, *150* (13), 2880−2892.

(22) Deng, F.; Wan, J.; Li, G.; Dong, H.; Xia, X.; Wang, Y.; Li, X.; Zhuang, C.; Zheng, Y.; Liu, L.; et al. Improved green and red GRAB sensors for monitoring spatiotemporal serotonin release in *vivo*. *Nat. Methods* **2024**, *21* (4), 692−702.

(23) Song, C.; Yu, W.; Wang, L.; Xi, X.; Zhang, X.; Wang, S.; Wen, W.; Wu, Z. Optical and electrochemical probes-assisted dual-mode nanosensor for ultrasensitive monitoring of serotonin in single cells. *Biosens. Bioelectron.* **2025**, *288*, No. 117845.

(24) Han, J.; Stine, J. M.; Chapin, A. A.; Ghodssi, R. A portable electrochemical sensing platform for serotonin detection based on surface-modified carbon fiber microelectrodes. *Anal. Methods* **2023**, *15* (9), 1096−1104.

(25) Huang, Z.; Lu, H.; Dong, H.; Chen, Z.; Lu, R.; Zhao, Y.; Du, Y.; Liu, Y.; Wu, Y.; Xu, M.; et al. Fe_3O_4/Ni nanoparticles anchored nitrogen-doped porous carbon derived from core-shell MOF for simultaneous electrochemical detection of dopamine and 5-hydroxytryptamine. *Talanta* **2025**, *286*, No. 127522.

(26) Zhu, F.; Xue, Y.; Ji, W.; Li, X.; Ma, W.; Yu, P.; Jiang, Y.; Mao, L. Galvanic Redox Potentiometry for Fouling-Free and Stable Serotonin Sensing in a Living Animal Brain. *Angew. Chem., Int. Ed.* **2023**, *62* (11), No. e202212458.

(27) Zhu, F.; Liu, Y.; Sun, Z.; Ni, J.; Jiang, Y. Aptamer-Based Galvanic Potentiometric Sensor for Real-Time Monitoring of Serotonin Signaling Under Psychosocial Stress. *Angew. Chem., Int. Ed.* **2025**, *64* (24), No. e202501701.

(28) Chen, L.; Cheng, C.; Chen, Y.; Wu, L.; Sun, T.; Xiong, Y. Constructing datasets and training deep networks for the direct

https://doi.org/10.1021/acsami.5c20971
ACS Appl. Mater. Interfaces XXXX, XXX, XXX−XXX

apoptotic cell identification from H&E staining images. *Oncol. Transl. Med.* **2025**, in press.
(29) Yan, D.; Jiao, L.; Chen, C.; Jia, X.; Li, R.; Hu, L.; Li, X.; Zhai, Y.; Strizhak, P. E.; Zhu, Z.; et al. p-d Orbital hybridization-engineered PdSn nanozymes for a sensitive immunoassay. *Nano Lett.* **2024**, *24* (9), 2912−2920.
(30) Liu, X.; Zhang, X.; Wei, D.; Liu, Z.; Yang, L. Innovative bioinspired hydrogel scaffolds enabling in-situ hybrid nanoflower integration for dual-mode acetylcholinesterase inhibitor profiling. *Biosens. Bioelectron.* **2025**, *271*, No. 117032.
(31) Rajarathinam, T.; Jayaraman, S.; Kim, C.-S.; Yoon, J.-H.; Chang, S.-C. Two-dimensional nanozyme nanoarchitectonics customized electrochemical bio diagnostics and lab-on-chip devices for biomarker detection. *Adv. Colloid Interface Sci.* **2025**, *341*, No. 103474.
(32) He, L.; Guan, C.; Bulushev, D. A.; Xiang, Q. Regulation of Metal-Support Interaction in Single-Atom Catalysis. *Small* **2024**, No. 2410976.
(33) Rastinfard, A.; Dalisson, B.; Barralet, J. Aqueous decomposition behavior of solid peroxides: Effect of pH and buffer composition on oxygen and hydrogen peroxide formation. *Acta. Biomater.* **2022**, *145*, 390−402.
(34) Wang, X.; Wei, G.; Liu, W.; Zhang, Y.; Zhu, C.; Sun, Q.; Zhang, M.; Wei, H. Platinum-Nickel nanoparticles with enhanced oxidase-like activity for total antioxidant capacity bioassay. *Anal. Chem.* **2023**, *95* (14), 5937−5945.
(35) Arshi, S.; Madane, K.; Shortall, K.; Hailo, G.; Alvarez-Malmagro, J.; Xiao, X.; Szymańska, K.; Belochapkine, S.; Ranade, V. V.; Magner, E. Controlled delivery of H_2O_2: A three-enzyme cascade flow reactor for peroxidase-catalyzed reactions. *ACS Sustainable Chem. Eng.* **2024**, *12* (28), 10555−10566.
(36) Ge, J.; Sun, X.; Li, X.; Yang, Y.; Zhang, L.; Qu, L.; Li, Z. Smartphone-assisted ultrasensitive colorimetric strategy based on Cu-CN single-atom nanozyme for acrylamide detection in fried food. *Food Chem.* **2025**, *490*, No. 145066.
(37) Feng, Y.; Shi, Y.; Zhao, Q.; Gao, G.; Wang, Z.; Zhi, J. Onion-like carbon based single-atom iron nanozyme for photothermal and catalytic synergistic antibacterial application. *J. Colloid Interface Sci.* **2025**, *681*, 205−214.
(38) Liu, F.; Jiao, F.; Wang, T.; Li, Z.; Song, H.; Wu, S.; Zhang, X.; Wang, H.; Chen, C.; Lu, Y., J. Free reactive oxygen species-independent dual enzymatic activity of iron single-atom catalyst for hydrogel-assisted portable visual analysis. *J. Colloid Interface Sci.* **2025**, *686*, 420−429.
(39) Chen, S.; Li, X.; Kao, C.-W.; Luo, T.; Chen, K.; Fu, J.; Ma, C.; Li, H.; Li, M.; Chan, T.-S.; et al. Unveiling the proton-feeding effect in sulfur-doped Fe-N-C single-atom catalyst for enhanced CO_2 electroreduction. *Angew. Chem., Int. Ed.* **2022**, *61* (32), No. e202206233.
(40) Cheng, H.; Chen, Y.; Liu, M.; Tao, H.; Chen, L.; Wang, F.; Huang, L.; Tang, J.; Yang, T.; Hu, R. Theory-guided design of S-doped Fe/Co dual-atom nanozymes for highly efficient oxidase mimics. *Chem. Sci.* **2024**, *15* (36), 14816−14828.
(41) Xie, Y.; Sun, F.; Chang, K.; Li, G.; Song, Z.; Huang, J.; Cheng, X.; Zhuang, G.; Kuang, Q. Axially coordinated gold nanoclusters tailoring Fe-N-C nanozymes for enhanced oxidase-like specificity and activity. *Adv. Sci.* **2024**, *11* (11), No. 2306911.
(42) Harati, J.; Wang, P. Leveraging integrative technologies to translate stem cell and cell reprogramming potential for neurodegenerative diseases. *Eur. Cell. Mater.* **2024**, *48*, 151−155.
(43) Chen, X.; Feng, M.; Xie, X.; Zhang, Y.; Zhang, J.; Yang, X. Fe single atoms anchored on fluorine-doped ultrathin carbon nanosheets for sensitive colorimetric detection of p-phenylenediamine. *Talanta* **2022**, *246*, No. 123487.
(44) Xie, X.; Wang, Y.; Zhou, X.; Chen, J.; Wang, M.; Su, X. Fe-N-C single-atom nanozymes with peroxidase-like activity for the detection of alkaline phosphatase. *Analyst* **2021**, *146*, 896.
(45) Niu, X.; Shi, Q.; Zhu, W.; Liu, D.; Tian, H.; Fu, S.; Cheng, N.; Li, S.; Smith, J. N.; Du, D.; et al. Unprecedented peroxidase-mimicking activity of single-atom nanozyme with atomically dispersed Fe-N_x moieties hosted by MOF derived porous carbon. *Biosens. Bioelectron.* **2019**, *142*, No. 111495.
(46) Wang, M.; Liu, L.; Xie, X.; Zhou, X.; Lin, Z.; Su, X. Single-atom iron containing nanozyme with peroxidase-like activity and copper nanoclusters based ratio fluorescent strategy for acetylcholinesterase activity sensing. *Sens. Actuators. B. Chem.* **2020**, *313*, No. 128023.
(47) Zhu, F.; Yu, Y.; Yu, Z.; Qiu, H.; Lu, G.-P.; Chen, Z.; Hu, J.; Lin, Y. S-Doping Regulated Iron Spin States in Fe-N-C Single-atom material for enhanced peroxidase-mimicking activity at neutral pH. *Small* **2024**, *20* (33), No. 2311848.
(48) Jiao, L.; Kang, Y.; Chen, Y.; Wu, N.; Wu, Y.; Xu, W.; Wei, X.; Wang, H.; Gu, W.; Zheng, L.; et al. Unsymmetrically coordinated single Fe-N_3S_1 sites mimic the function of peroxidase. *Nano Today* **2021**, *40*, No. 101261.
(49) Jia, Y.; Xiong, X.; Wang, D.; Duan, X.; Sun, K.; Li, Y.; Zheng, L.; Lin, W.; Dong, M.; Zhang, G.; et al. Atomically dispersed Fe-N_4 modified with precisely located S for highly efficient oxygen reduction. *Nano-Micro Lett.* **2020**, *12* (1), 116.
(50) Niu, X.; Xu, X.; Li, X.; Pan, J.; Qiu, F.; Zhao, H.; Lan, M. Surface charge engineering of nanosized CuS via acidic amino acid modification enables high peroxidase-mimicking activity at neutral pH for one-pot detection of glucose. *Chem. Commun.* **2018**, *54*, 13443−13446.
(51) He, Y.; Li, X.; Xu, X.; Pan, J.; Niu, X. A cobalt-based polyoxometalate nanozyme with high peroxidase-mimicking activity at neutral pH for one-pot colorimetric analysis of glucose. *J. Mater. Chem. B* **2018**, *6*, 5750−5755.
(52) Han, L.; Li, C.; Zhang, T.; Lang, Q.; Liu, A. Au@Ag heterogeneous nanorods as nanozyme interfaces with peroxidase-like activity and their application for one-pot analysis of glucose at nearly neutral pH. *ACS Appl. Mater. Interfaces* **2015**, *7*, 14463−14470.
(53) Chen, Q.; Li, S.; Liu, Y.; Zhang, X.; Tang, Y.; Chai, H.; Huang, Y. Size-controllable Fe-N/C single-atom nanozyme with exceptional oxidase-like activity for sensitive detection of alkaline phosphatase. *Sens. Actuators. B. Chem.* **2020**, *305*, No. 127511.
(54) Chen, Y.; Jiao, L.; Yan, H.; Xu, W.; Wu, Y.; Zheng, L.; Gu, W.; Zhu, C. Fe-N-C Single-atom catalyst coupling with Pt clusters boosts peroxidase-like activity for cascade-amplified colorimetric immunoassay. *Anal. Chem.* **2021**, *93* (36), 12353−12359.
(55) Zhu, F.; Lu, G.-P.; Wang, F.; Ren, E.; Yu, Y.; Lin, Y. Iron catalyzed organic reactions in water: A "nature-like" synthesis. *Curr. Opin. Green Sustainable Chem.* **2023**, *40*, No. 100754.

https://doi.org/10.1021/acsami.5c20971
ACS Appl. Mater. Interfaces XXXX, XXX, XXX−XXX